ACS APPLIED MATERIALS & INTERFACES

www.acsami.org

Research Article

Bio-Inspired Untethered Robot-Sensor Platform for Minimally Invasive Biomedical Sensing

Yizong Li, Amro Halwah, Shah R. A. Bhuiyan, and Shanshan Yao*

Cite This: *ACS Appl. Mater. Interfaces* 2023, 15, 58839−58849

Read Online

ACCESS | Metrics & More | Article Recommendations | Supporting Information

ABSTRACT: Conventional catheter- or probe-based in vivo biomedical sensing is uncomfortable, inconvenient, and sometimes infeasible for long-term monitoring. Existing implantable sensors often require an invasive procedure for sensor placement. Untethered soft robots with the capability to deliver the sensor to the desired monitoring point hold great promise for minimally invasive biomedical sensing. Inspired by the locomotion modes of snakes, we present here a soft kirigami robot for sensor deployment and real-time wireless sensing. The locomotion mechanism of the soft robot is achieved by kirigami patterns that offer asymmetric tribological properties that mimic the skin of the snake. The robot exhibits good deployability, excellent load capacity (up to 150 times its own weight), high-speed locomotion (0.25 body length per step), and wide environmental adaptability with multimodal movements (obstacle crossing, locomotion in wet and dry conditions, climbing, and inverted crawling). When integrated with passive sensors, the versatile soft robot can locomote inside the human body, deliver the passive sensor to the desired location, and hold the sensor in place for real-time monitoring in a minimally invasive manner. The proof-of-concept prototype demonstrates that the platform can perform real-time impedance monitoring for the diagnosis of gastroesophageal reflux disease.

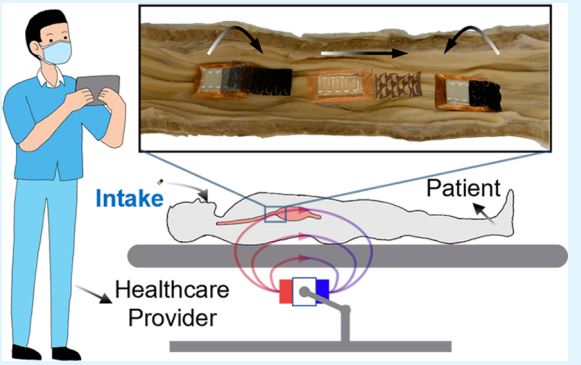

KEYWORDS: *soft robots, kirigami, bioinspiration, biomedical sensing, passive sensors, gastroesophageal reflux diagnosis*

1. INTRODUCTION

Close monitoring of health parameters facilitates early diagnosis and provides effective therapeutic guidance.[1−3] The conventional catheter or probe-based monitoring is uncomfortable and inconvenient, making it infeasible for frequent monitoring.[4,5] When used for continuous monitoring, the procedures are not risk-free and can result in inaccurate readings if patients' daily activities are affected by the presence of the invasive probe.[6] Recently developed implantable sensors, used as an alternative, often require invasive procedures to place the sensors in desired locations.[3,5−10] Therefore, a minimally invasive method of biomedical monitoring is in urgent demand.

Bio-inspired untethered soft robots that possess the capability to deliver sensors precisely to target areas offer significant promise for advancing minimally invasive biomedical monitoring..[11−13] A wealth of inspiration has been drawn from various living organisms in the design of soft robots.[12,14−26] Among the commonly observed biological structures, the design of soft robots has frequently incorporated leg structures.[27,28] The multilegged soft robot demonstrated potential applications in drug delivery, temperature sensing, and tapping sensing.[27,28] However, the multilegged soft robot has yet to explore the capability of vertical and inverted crawling, desired features for navigating the intricate structures inside the human body.[27] Additionally, the wireless sensing circuit is complex, necessitating the incorporation of a rigid printed circuit board.[28] The remarkable climbing abilities of geckos have garnered significant attention, leading to the development of several soft robots inspired by the gecko's footpad.[29,30] Nevertheless, these robots have a limited climbing distance, as the adhesion between the robot footpad and tissue surface is weak and diminishes quickly, particularly when considering the viscous surface inside the human body.[29] Snakes possess a remarkable and adaptable capability of limbless locomotion enabling them to navigate and thrive in various terrains, including deserts, forests, and mountains.[31−35] The limbless locomotion strategy allows us to emulate snake-like movements through a single actuator.[36,37] This singular actuation approach not only simplifies the control mechanisms but also facilitates size reduction, which is important for minimally invasive biomedical applications. Several soft robots have already been inspired by the locomotion mechanism of

Received: September 7, 2023
Revised: November 25, 2023
Accepted: November 26, 2023
Published: December 5, 2023

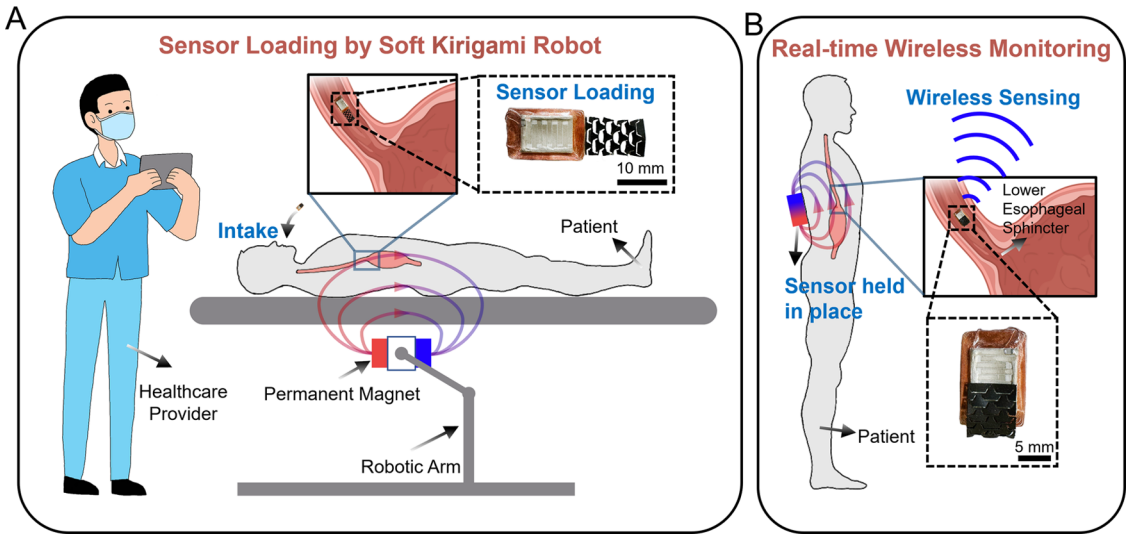

Figure 1. Schematics of integrated soft robot-sensor platform for GERD monitoring. (A) The patient intakes the integrated robot-sensor with the robot folded on top of the sensor. A healthcare provider controls a permanent magnet by a robotic arm to unfold the robot and steer the integrated robot-sensor to the monitoring point. (B) The robot is flipped upside down and holds the sensor in place by a permanent magnet mounted on the external skin surface. A reader attached to the skin surface is used to wirelessly collect real-time data from the passive sensor.

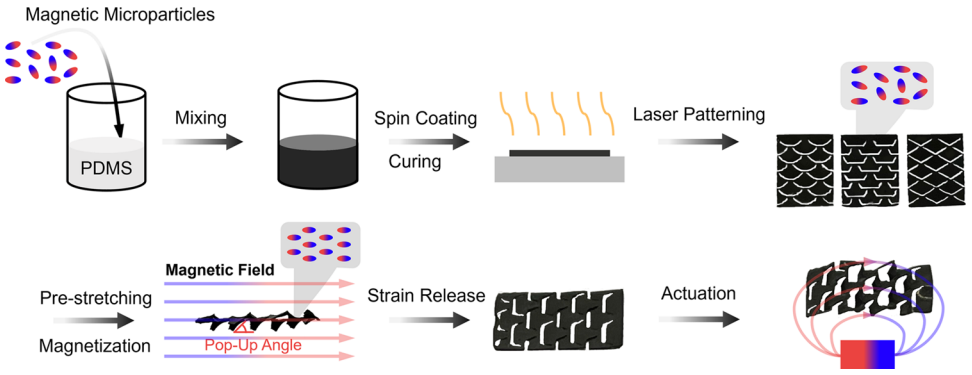

Figure 2. Fabrication process of bio-inspired kirigami-based soft robots.

snakes and developed using the pneumatic actuation method.[17,36,37] Nevertheless, these soft robots have faced limitations in terms of environmental adaptability, and the presence of tethered connections, which makes them less suitable for noninvasive or minimally invasive biomedical sensing.[18,38,39] Moreover, high load capacity and agile maneuverability are crucial for efficient sensor delivery.[11,12,27] It is still challenging for existing bio-inspired untethered soft robots to achieve all desired characteristics for biomedical sensing, including high-speed locomotion, wide environmental adaptability, and high load capacity (Table S1). All of these are essential for biomedical sensing in the intricate and dynamically changing environments within the human body.[11,12,39]

To overcome these challenges, we report a bio-inspired magnetically actuated soft kirigami crawling robot with agile maneuverability and flexibility to operate in constricted spaces, as shown in Figure 1. The soft robots are designed to mimic the functionality of snake skin. Under the actuation of a permanent magnet, the snake-inspired kirigami pattern undergoes a transformation from a two-dimensional (2D) to three-dimensional (3D) configuration. The pop-up 3D pattern is directional and can provide anisotropic friction that enables forward motion. By optimizing the kirigami patterns and employing both magnetic force and torque, the robot can achieve good deployability, high-speed locomotion (0.25 body length (BL) per step), excellent load capacity (up to 150 times its own weight), and versatile locomotion modes (e.g., obstacle crossing, locomotion in wet and dry conditions, climbing, and inverted crawling). Toward real-world biomedical applications, an integrated soft robot-sensor system has been developed, which consists of a soft robot for locomotion and a passive impedance sensor for real-time wireless sensing. The integrated robot-sensor system was demonstrated for the wireless monitoring of gastroesophageal reflux disease (GERD) in a minimally invasive manner.

2. RESULTS AND DISCUSSION

2.1. Design and Fabrication of the Soft Kirigami Robot. The rectilinear locomotion mode stands out as an efficient means of movement for snakes when navigating in confined spaces, which aligns well with the requirement of minimally invasive monitoring.[40] Herein, we adopted this specific locomotion mode as inspiration for the design of the soft robot. Specifically, during the rectilinear locomotion of snakes, part of the snake's body acts as an anchor point, facilitated by anisotropic scales.[37,40−43] This adaptation enables snakes to maintain a grip on the substrate and propel its body

https://doi.org/10.1021/acsami.3c13425
ACS Appl. Mater. Interfaces 2023, 15, 58839−58849

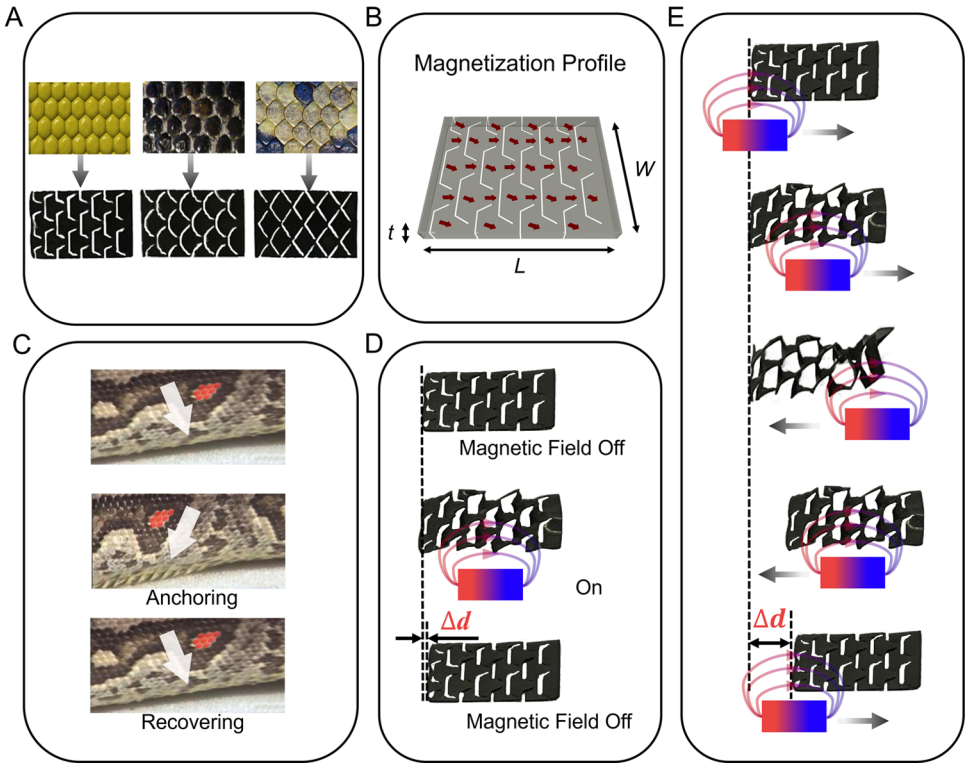

Figure 3. Design of the soft kirigami robot and mechanisms of two locomotion modes. (A) Comparisons between different patterns of snake skins and kirigami patterns. (B) Magnetization profiles of the soft robot. Arrows indicate magnetization direction. (C) Snapshots showing the rectilinear locomotion mode of a snake and the anisotropic friction introduced by anchoring the snake skin (video courtesy of H. Marvi and D. Hu). (D, E) Schematics of two actuation methods.

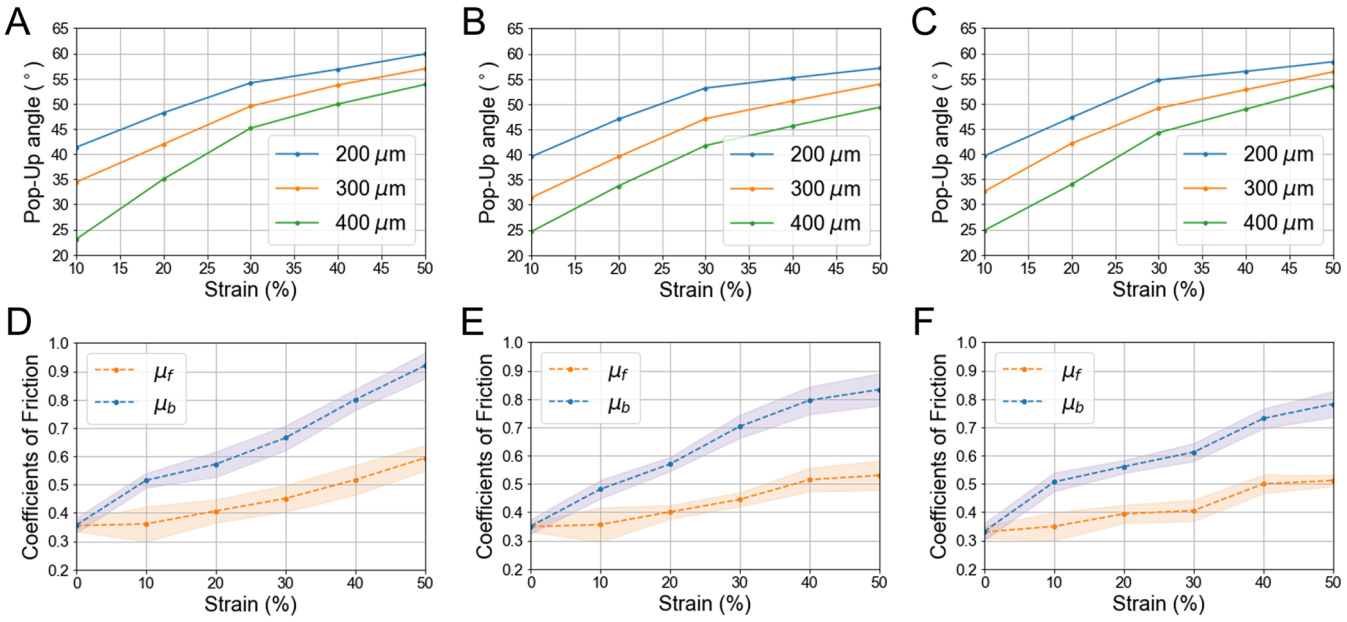

Figure 4. Characterization of kirigami crawlers. Pop-up angles of kirigami patterns with different thicknesses as a function of strain for (A) trapezoidal kirigami, (B) circular kirigami, and (C) triangular kirigami. The forward (μ_f) and backward (μ_b) COF as a function of strain for kirigami robots with (D) trapezoidal kirigami, (E) circular kirigami, and (F) triangular kirigami. The thickness of soft robots is 200 μm.

forward without sliding backward.[40−43] Then, the rest of the snake's body moves forward due to its high stretchability and flexibility.[40−43] During movement, the snake skin is tuned to exert high friction for propelling, or low friction for sliding along the substrate.[44] To achieve the asymmetric friction that propels the body to move forward, a kirigami skin was designed to mimic the snake skin. The kirigami skin is fabricated by mixing magnetic microparticles and polymer precursor, spin-coating the mixture to form a thin film, and laser cutting the cured thin film into designed kirigami patterns (Figures 2 and 3). When stretching the kirigami skin, the kirigami pattern undergoes a transformation from 2D to 3D

https://doi.org/10.1021/acsami.3c13425
ACS Appl. Mater. Interfaces 2023, 15, 58839−58849

configurations. The pattern pops up, which produces asymmetric friction (i.e., the forward friction is smaller than the backward friction, as shown in Figure S1). Then, the key is how to mechanically stretch the kirigami skin with noncontact magnetic fields. To impart such mechanical stimuli required for crawling, an anisotropic magnetization profile was introduced during the magnetization process. After laser patterning, the resulting kirigami skin was pre-stretched and magnetized in a Halbach array with a magnetic field of 1.2 T (Figure 2). Then, the pre-stretch was released, resulting in an anisotropic magnetization profile, as shown in Figure 3B. Once the magnetic field is applied again, the magnetic dipole tends to align with the magnetic field. The pop-up angle then introduces anisotropic friction. By exploiting this asymmetric friction induced by stretching and releasing the kirigami skin, the soft robot is inclined to move in the direction in which friction is larger.

2.2. Analysis of Robot Locomotion. The kirigami robot could be actuated with a permanent magnet. Magnetic torque and magnetic force are applied to the kirigami robot due to the magnetic field generated by a permanent magnet. The torque aligns the soft robot with the applied magnetic field, forces the kirigami pattern to buckle out in the out-of-plane direction, and therefore raises the body of the soft robot. The magnetic force pulls the soft robot to move to the local maximum magnetic field. More details in the analysis of the magnetic torque and force are provided in the Supporting Information.

By mimicking the snake skin and the locomotion of the snake (Figure 3C−E), the movement of the kirigami robot can be divided into two phases: stretching and recovery processes. Before the stretching process (without the magnetic field), the kirigami robot can be recognized as a thin film that can slide in both forward and backward directions. During the stretching process induced by the magnetic field, the kirigami cut buckles out of the plane, changing the friction property of the soft kirigami robot. The pop-up kirigami pattern results in a significant increase in the coefficient of friction (COF) in the backward direction. As illustrated in Figure 4A−C, as the strain increases, the pop-up angle increases, accompanied by more obvious 3D deformations. Thinner kirigami skin leads to larger pop-up angles. As a result of the increased pop-up angle, the COF increases in both backward and forward directions, and the difference between backward COF and forward COF becomes larger (Figure 4D−F). Among different kirigami patterns (i.e., trapezoidal, circular, and triangular patterns), trapezoidal patterns exhibit the largest pop-up angle and COF.

In the strain recovery process induced by turning off or reversing the magnetic field, the kirigami cut buckles back inward until the kirigami robot becomes a thin film. The asymmetric COF in the forward and backward directions also gradually recovered. The change in the friction properties affects the locomotion of the soft kirigami robot by shifting the position of the anchor point (Figures 3C and S3). The location of the anchor point in the stretching process and recovery process can be calculated as[37]

$$\left(\frac{A}{L}\right)_{\text{stretch}} = -\frac{1}{2}\left(\frac{\mu_b - \mu_f}{\mu_b + \mu_f}\right) \tag{1}$$

$$\left(\frac{A}{L}\right)_{\text{recovery}} = \frac{1}{2}\left(\frac{\mu_b - \mu_f}{\mu_b + \mu_f}\right) \tag{2}$$

where A is the distance between the center of the soft kirigami robot and the anchor point, L represents the length of the soft robot, and μ_f and μ_b indicate the COF in the forward and backward directions, respectively. At the beginning of the stretching, the anchor point is located at the center of the soft kirigami robot. Therefore, the soft kirigami robot extends equally at the head and tail, as shown in Figure S4A. As the body of the soft kirigami robot extends, the kirigami pattern starts to buckle outward and the COF changes. The COF increases in both the forward and backward directions. The COF in the backward direction increases more rapidly than that in the forward direction. The anchor point starts to move back toward the tail of the kirigami robot. This backward shift of the anchor point leads to an asymmetric extension of the soft kirigami robot. The soft kirigami robot extends more at the head than it does at the tail (Figure S4A). When the robot begins to recover, which is controlled by turning off or reversing the magnetic field, the anchor point jumps to a position between the center and the head of the soft-body robot. The position of the anchor point leads to a greater contraction of the soft robot at its tail than at its head (Figure S4A). The total displacement (Δd) of the soft kirigami robot in one step can be calculated using the following expression[37]

$$\Delta d = L_0\left[-\int_0^{\varepsilon_{\max}}\left(\frac{A}{L}\right)_{\text{stretch}} d\varepsilon + \int_{\varepsilon_{\max}}^{0}\left(\frac{A}{L}\right)_{\text{recovery}} d\varepsilon\right] \tag{3}$$

where L_0 is the initial length of the soft robot, and ε and $\varepsilon_{\max}$ represent the strain of the soft robot and the strain corresponding to the maximum extension of the soft robot, respectively.

The kirigami robot with an asymmetric COF can be actuated by a permanent magnet. Two actuation modes are investigated, as presented in Figure 3D,E. In the first on/off actuation mode (Figure 3D), a bar magnet is put underneath the soft robot to make the soft robot stretch, and then the magnet is moved away from the kirigami robot to recover the tensile strain. Nevertheless, in the on/off mode, the applied magnetic field from the permanent magnet induces only a small strain (9%) on the kirigami robot. As a result, the difference in the COF between the forward and backward directions is small, and the anchor point is very close to the center of the kirigami robot. It is also implied that the moving speed can be optimized by adjusting the direction and magnitude of the applied magnetic field. From Figure S4A and eq 3, the total displacement in one step can be simplified as

$$\Delta d = [(\Delta d_3 -) + (\Delta d_4 -)] - [(\Delta d_1 -) + (\Delta d_2 -)] \tag{4}$$

or

$$\Delta d = [(\Delta d_1 +) + (\Delta d_2 +)] - [(\Delta d_3 +) + (\Delta d_4 +)] \tag{5}$$

Equations 4 and 5 imply that the moving speed can be optimized by minimizing Δd_1-, Δd_2-, Δd_3+, and Δd_4+ and maximizing Δd_3-, Δd_4-, Δd_1+ and Δd_2+.

To optimize the moving speed, another actuation mode, the reciprocating actuation mode, is introduced. As shown in Figures 3E and S4B, the magnet is put below the kirigami robot and moved toward the direction of locomotion. As the magnet moves forward, the magnetic field applied to the

https://doi.org/10.1021/acsami.3c13425
ACS Appl. Mater. Interfaces 2023, 15, 58839−58849

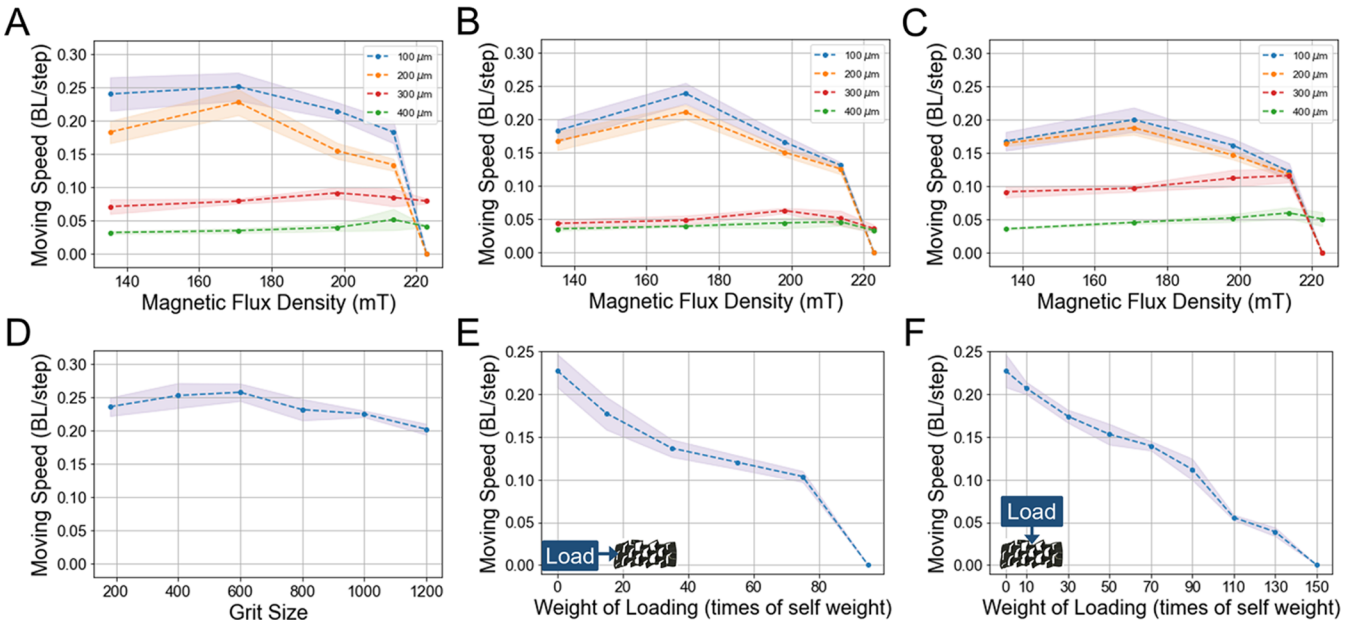

Figure 5. Moving speed of kirigami crawlers with the second reciprocating actuation mode. The moving speed of kirigami robots with different thicknesses as a function of magnetic flux density for (A) trapezoidal pattern, (B) circular pattern, and (C) triangular pattern. (D) Moving speed of kirigami robots on sandpapers with different grit sizes. Moving speed as a function of the weight of loadings for (E) dragging and (F) carrying loads. The thickness of the soft robot is 200 μm. The abbreviation BL represents body length.

kirigami robot gradually changes from parallel to the substrate to a certain angle to the substrate. Magnetic torque bends the head of the kirigami robot upward, and meanwhile, the magnetic force pulls the kirigami robot for stretching (Figure S5). The kirigami cut buckles outward to align with the magnetic flux and balance the magnetic force. The magnet bar is moved forward until the tail is on the verge of sliding when the anchor point is at the tail of the kirigami robot. As a result, Δd_1- and Δd_2- are equal to 0. Then, the magnet is moved backward, resulting in the recovery of the kirigami robot, as shown in Figure 3E. The anchor point is located where the robot bends (Figure S4B). The closer the anchor point is to the head of the robot, the faster the moving speed of the robot can be achieved, as shown in eqs 4 and 5. The stretched length (i.e., Δd_1+ and Δd_2+) and the anchor point during the recovery process are associated with the thickness of the robot and the applied magnetic flux density. Therefore, to improve the moving speed, the effects of thickness and applied magnetic flux density are investigated. As shown in Figure 5A–C, the moving speed is increased at a reduced thickness of the kirigami robot except for a very large magnetic flux density. If the applied magnetic field is too large, kirigami robots would be attracted to the magnet by the strong magnetic force, resulting in a lower moving speed. Conversely, insufficient magnetic fields produce limited stretching of the kirigami robot, consequently impeding its locomotion. A suitable applied magnetic flux density is essential to achieve a high moving speed. When Δd_1- and Δd_2- are zero, Δd_1+ and Δd_2+ that the soft kirigami robot can achieve are determined by the forward COF. A larger forward COF at the tail leads to more stretching in the robot head before the tail starts to slide. Since the trapezoidal kirigami pattern possesses the largest forward COF, the soft robot with the trapezoidal kirigami pattern can achieve the maximum moving speed (0.25 BL/step). Table S1 shows a comparison with existing magnetic crawlers in the literature in terms of moving speed, adaptability, and real-world applications. Because the reported magnetic robots were driven at different actuation frequencies, the moving speed is normalized to BL per step to have a fair comparison. The reported soft robot meets all desired requirements for biomedical sensing. The fast-moving speed and high loading capacity are important for steering sensors efficiently to the designated location. The agile maneuverability and adaptability to different environments and terrains are especially conducive for biomedical applications where the crawling environment is complex and diverse.

2.3. Robot Locomotion in Various Environments. To demonstrate the snake-like versatility of the developed soft kirigami robot, locomotion experiments were performed in various environments (Movie S1). To imitate the complex topography in biological environments during biomedical sensing, the moving speed of the soft kirigami robot was tested on sandpaper of different roughnesses (Figure 5D). The results indicate that the soft kirigami robot is able to move effectively on the sandpaper without a significant decrease of speed. Load capacity is an essential parameter in determining the potential applications of soft robots, such as cargo delivery.[20,27,29] As shown in Figure 5E,F, the soft kirigami robot is capable of dragging loads on its tail and carrying loads on top. The maximum load-carrying capacity of the robot was 150 times its weight, while the maximum load-dragging capacity was 90 times its weight.

As shown in Figures S4B and S5, the magnetic force applied to the soft crawling robot results in a normal force exerted by the substrate, which counterbalances the magnetic force. This generates sufficient friction to allow for the continuous movement of the soft kirigami robot over complex terrains. The capability of snakes to traverse gaps and crawl on tree trunks was mimicked by the soft kirigami robot (Figure 6A–D). Figure 6A shows that the soft kirigami robot can cross a 2 mm wide gap. The soft kirigami robot can move in multiple directions on surfaces with varying slopes, including

https://doi.org/10.1021/acsami.3c13425
ACS Appl. Mater. Interfaces 2023, 15, 58839–58849

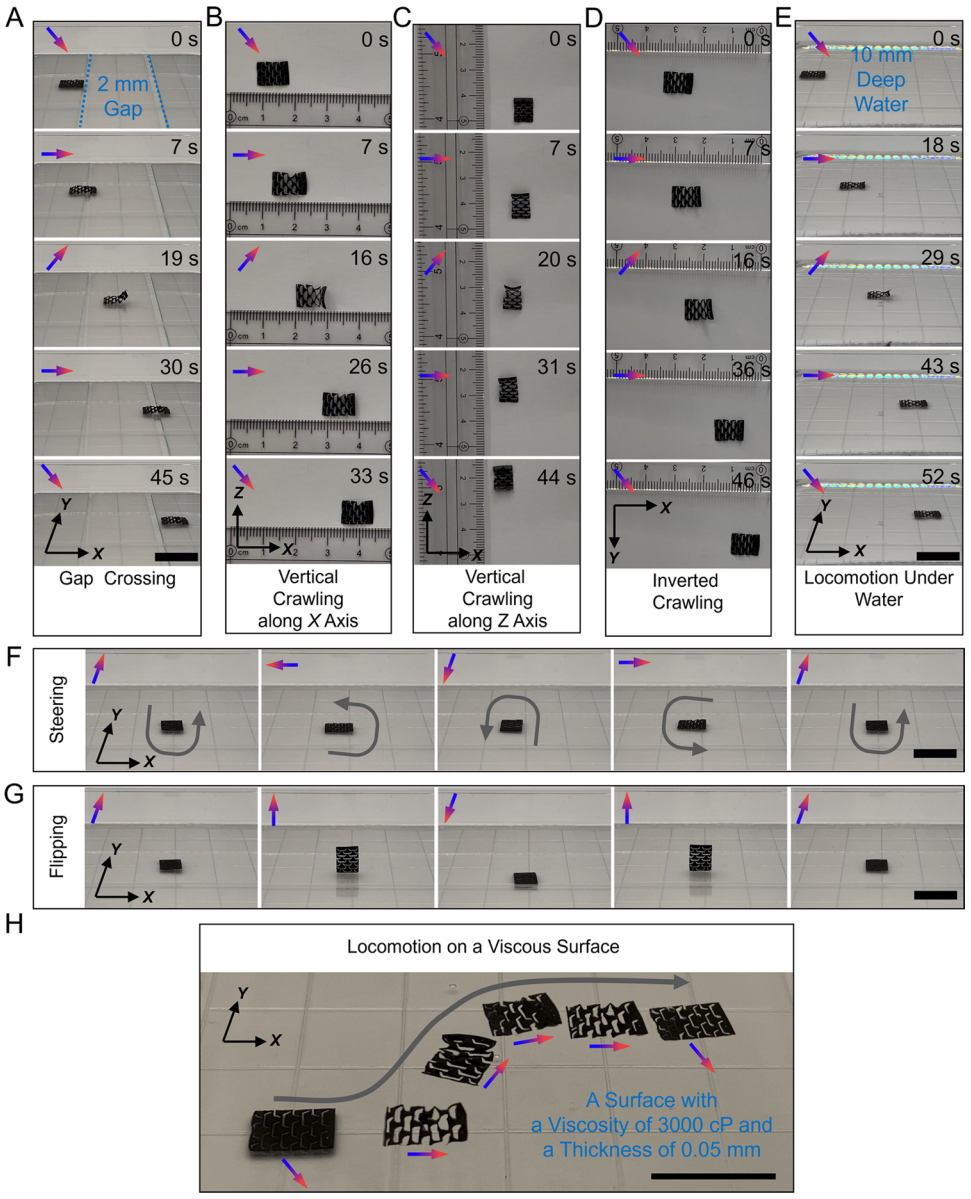

Figure 6. Multimodal locomotion of kirigami robots in different environments. The soft robot is capable of (A) crossing a gap, (B) moving on a vertical wall along the *X* axis, (C) moving on a vertical wall along the *Z* axis, (D) inverted crawling, (E) locomotion under water, (F) turning in all directions for steering, (G) flipping upside down for deploying, and (H) locomotion on a viscous surface. The blue-red arrows indicate the direction of the applied magnetic field at the center of the soft kirigami robot. Scale bars, 15 mm.

perpendicular walls, as shown in Figure 6B,C. Additionally, the soft kirigami robot is able to overhang and move inversely on surfaces (Figure 6D). The adaptability of the soft kirigami robot to various environments was further demonstrated by its ability to move in wet environments (Figures 6E,H and 7A). Despite a reduction in moving speed in wet environments, the soft kirigami robot is capable of locomoting in the water, as well as traversing a 0.05 mm thick viscous surface possessing a viscosity of 3000 cP. It is noteworthy that the viscosity of the experimental surface surpasses the typical viscosity of mucus within the human esophagus (130 cP).[45] These capabilities demonstrate the soft kirigami robot's snake-like adaptability to complex environments, including dry environments, wet environments, undulated topography, and surfaces with different slopes. The soft Kirigami robot also exhibits superior steering capability and deployability, with the ability to be steered in all directions and flipped upside down, as shown in Figure 6F,G. In summary, with adaptability, maneuverability, and load capacity, the soft kirigami robot shows great potential in real-world applications where locomotion in complex environments and good load capability are necessary.[46] In the following section, an integrated robot-sensor platform for biomedical sensing is demonstrated.

2.4. Integrated Soft Robot-Sensor Platform and Application in the Diagnosis of GERD. As one of the most common gastrointestinal diseases, GERD affects people of all ages, with a global prevalence of 2.5−33%.[47−49] Acid regurgitation, heartburn, chest discomfort, odynophagia, burping, nausea, and vomiting are symptoms of GERD.[50] These symptoms significantly lower the quality of life. As the disease worsens, GERD can also cause Barrett's esophagus and even esophageal cancer.[48] Monitoring esophageal reflux is an effective way for diagnosing GERD.[48] Traditionally, a catheter is delivered to the patient's esophagus through the patient's

https://doi.org/10.1021/acsami.3c13425
ACS Appl. Mater. Interfaces 2023, 15, 58839−58849

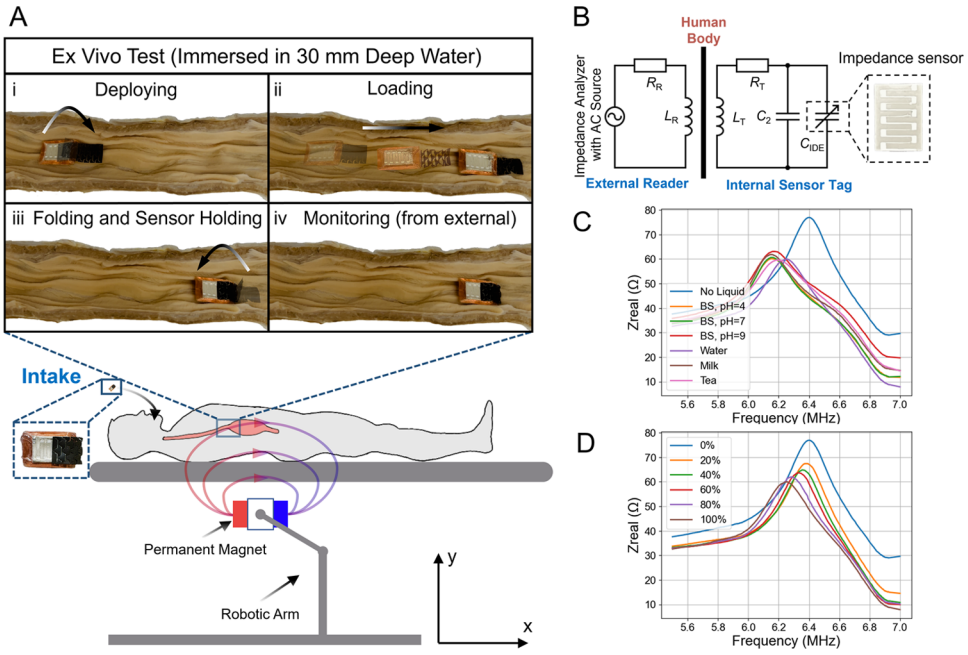

Figure 7. Integrated soft robot-sensor platform for GERD monitoring. (A) After intaking the soft robot integrated with the IDE sensor, the robot is deployed (i), and then the IDE sensor is dragged by the soft robot (steered by an external magnet) to the desired sensing location (ii). (iii) The soft robot is flipped upside down and holds the sensor in place. (iv) Real-time wireless monitoring is performed using a reader attached to the external skin surface. Experiments in (A) were performed on the pig esophagus immersed in 30 mm water. The external reader coil was ignored for clarity. (B) Equivalent circuit of the reader and the sensor tag. (C) Resonant frequency shifts when different types of liquid are in contact with the IDE sensor (to mimic the gastroesophageal reflex from the stomach). (D) Measured real part of impedance from the external reader when the sensor was immersed in different levels of water. The water level is indicated by the percentage of the total height of the IDE sensor. The abbreviation BS represents buffer solution. A segment of the pig esophagus was introduced between the IDE sensor and the reader. The distance between the sensor tag and the reader is around 30 mm.

nose or mouth and then is held in place to measure esophageal acidity for 24 h.[47] However, it is reported that 10% of patients refuse to take the monitoring and 4% of patients could not tolerate the discomfort caused by the catheter.[6,51] Moreover, the discomfort of the catheter can change the patient's daily eating habits and routine, which can affect the observation results.[47] Another way to monitor esophageal reflux is by using a wireless sensing capsule that can achieve wireless esophageal reflux monitoring by integrated sensors. This method offers greater comfort and fewer restrictions on daily activities compared to traditional catheter-based methods.[6,52−55] The wireless sensing capsule is typically introduced into the gastrointestinal tract either via catheter-based delivery or swallowing accompanied by natural peristaltic waves.[6,54,56,57] Nevertheless, catheter-based delivery can elicit unfavorable side effects, including throat pain, cough, and esophageal discomfort. Capsule delivery relying on natural movements can lead to incomplete or inaccurate results due to the capsule's limited mobility, which may impede delivery to the designated area.[54,57] Moreover, the constrained mobility and rigid body of the capsule increase the chance of being entrapped within the gastrointestinal tract, leading to blockage. Sometimes surgical interventions are necessitated to remove the entrapped capsule.[56,57] Hence, a controllable noninvasive way to deliver sensors for GERD diagnosis is needed. Here, a swallowable soft device consisting of a soft kirigami robot and a passive sensor is developed (Figure 1). As shown in Figure 7, once swallowed, the soft kirigami robot can be deployed and steered to the desired sensing location on the esophageal wall, and the passive sensor can be secured to perform wireless monitoring of esophageal impedance, a crucial diagnostic parameter for GERD.[47,48,58]

The passive impedance sensor exploits capacitive sensing and passive inductive coupling. As shown in Figures 1 and 7, the sensor consists of two parts: (1) A sensor tag part placed internally on the esophageal wall that contains a screen-printed interdigitated impedance sensor, a planar inductive coil, and a 100 pF surface mount capacitor. (2) An external reader with a planar inductive coil connected to the impedance analyzer. Due to its passive nature, no battery and complex circuitry are needed for the internal sensor tag, and no wired connection is necessary between the internal sensor tag and the external reader. The overall sensor tag size is 15 mm × 10 mm, as shown in Figure S6A. When integrated with the soft kirigami robot that can be folded on top, the overall dimension of the robot-sensor platform is 18 mm long and 10 mm wide, which can be swallowed without difficulties.[7]

The impedance sensor is designed as an interdigitated electrode (IDE) coated with a thin layer of poly(dimethylsiloxane) (PDMS)/$BaTiO_3$ composites. Introducing $BaTiO_3$ into the PDMS helps increase the dielectric permittivity, as shown in Figure S6B. A 20-turn coil with an inductance of L_T is connected in parallel with the IDE sensor. A surface-mounted 100 pF capacitor (C_2) is also placed in parallel with the coil and the IDE sensor to reduce the resonant frequency of the sensor tag. To monitor the impedance change due to the esophageal reflux, the impedance analyzer is connected to the reader (i.e., a hand-wound planar coil). The sensor tag is separated from the reader while coupled by passive inductive coupling. The equivalent circuit is shown in Figure 7B. The measured real part of the impedance

https://doi.org/10.1021/acsami.3c13425
ACS Appl. Mater. Interfaces 2023, 15, 58839−58849

(Re{Z_R}) and resonant frequency (f_R) from the reader can be expressed as[59−61]

$$\mathrm{Re}\{Z_R\} = R_R + 2\pi f L_R k^2 Q_T \frac{\frac{f}{f_T}}{1 + Q_T{}^2\left(\frac{f}{f_T} - \frac{f_T}{f}\right)^2} \quad (6)$$

$$f_R = \frac{2Q_T}{\sqrt{4Q_T{}^2 - 2}} f_T \quad (7)$$

where R_R is the resistance and L_R is the inductance of the reader, and k is the coupling coefficient. Z_T, f_T, and Q_T are the impedance, resonant frequency, and quality factor of the sensor tag, respectively. Since $Q_T \gg 1$, f_R can be simplified as

$$f_R \approx \frac{1}{2\pi\sqrt{L_T C_T}} \quad (8)$$

where C_T is the capacitance of the sensor tag ($C_T = C_1 + C_2$). From eq 6, the resonant frequency of the reader measured by the impedance analyzer is determined by the resonant frequency of the tag. When acid or nonacid reflux occurs, the medium surrounding the sensor tag changes from air to liquid. The overall capacitance of the IDE will increase due to the increased dielectric permittivity. As a result, the resonant frequency of the sensor tag will shift to a lower frequency. Due to the inductive coupling, such a resonant frequency shift can be reflected in the frequency shift measured from the external reader (Figure S7). More analysis of the IDE sensor and the coupling of the sensor and tag are provided in the Supporting Information.

To demonstrate the practical applications, the entire device, including the soft robot and the sensor tag, is designed to be biocompatible for in vivo monitoring. The biocompatibility of NdFeB/PDMS composites employed in the fabrication of the soft robot has been previously validated in cell viability tests for a duration of 24 h.[62] In addition, a thin film of PDMS was coated to encapsulate the sensor tag, thereby ensuring the sensor tag's biocompatibility. We then conducted an ex vivo evaluation of the robot-sensor platform for monitoring GERD (Movie S2). A pig esophagus immersed in water to a depth of 30 mm was employed to emulate real-world conditions. It is noteworthy that the water depth used in this experiment exceeds the average lumen diameter of the human esophagus (20 mm).[63] A hand-held magnet that can generate sufficient magnetic flux density (around 170 mT) at a distance of 30 mm was used to deploy, actuate, and hold the robot-sensor platform during the test. As shown in Figure 7A, the integrated robot-sensor with the kirigami robot folded on top of the sensor can be swallowed. The kirigami robot can then be unfolded and steered by an external magnet toward the monitoring point (around 50 mm above the lower esophageal sphincter).[6] After arriving at the monitoring point, the kirigami robot is flipped upside down to hold the sensor in place by an external permanent magnet for 24 h GERD monitoring. Note, in real applications, the robot-sensor device can be monitored and guided using ultrasound.[20,64] The retention test demonstrates that the platform can be reliably attached to the esophagus by a permanent magnet with a slight sliding of only 2.5 mm (Figure S8). Notably, the robot-sensor platform did not exhibit any signs of detachment, damage, or degradation throughout the ex vivo experiment (Figure 7A), retention test (Figure S8), and the subsequent 24 h stability test in an acidic environment of pH = 1 (Figure S9), enabling an uninterrupted 24 h GERD monitoring. The presence of permanent magnets may raise concerns about their impact on daily activities. This can be addressed by encapsulating the magnet's outer surfaces (except the surface in contact with the skin) with magnetic shield layers. After the shield layers were applied, the magnetic field from the side of the magnet covered with shield layers is minimized (Figure S10). Meanwhile, the magnetic field from the unshielded side of the magnet remains nearly unaltered, ensuring the retention of the robot-sensor platform.

Different types of liquids were used to mimic the gastroesophageal reflex, including water, milk, tea, and pH buffer solutions. As expected, when there is a reflex, the measured resonant frequency shifts to the lower frequency (Figure 7C) and can be detected at a maximum distance of 40 mm, which is sufficient for GERD monitoring.[52,53] The frequency shift is related to the amount of liquid on the IDE sensor, and a small amount of liquid can be detected by the sensor (Figure 7D). Overall, the developed robot-sensor system is small, minimally invasive, and does not need a catheter or other types of wired connection for real-time GERD monitoring.

3. CONCLUSIONS

In this work, we have demonstrated a snake-inspired kirigami-based soft magnetic robot with agile maneuverability, good load capacity, and wide adaptability to different environments. The kirigami pattern is designed by mimicking snake skin to generate high friction to propel itself. The anisotropic magnetization profile required for magnetic actuation is introduced by pre-stretching during the magnetization process. It is found that the out-of-plane deformation of the kirigami pattern leads to the difference in the COF in the forward and backward directions, which plays a vital role in the moving speed of the kirigami robot. The applied magnetic field and thickness of the kirigami robot also affect the moving speed. The actuation method was optimized by employing both magnetic force and magnetic torque to improve the moving speed. The resulting kirigami robots are capable of steering in all directions and deployable, moving in water, crossing gaps, moving vertically, and moving on an inverted wall. Finally, a new robot-sensor platform was developed that consisted of a magnetic kirigami robot and a wireless passive sensor. The integrated robot-sensor platform paves the way for real-time wireless biomedical sensing in a minimally invasive manner. The main contributions of this work include: (1) The development of snake-inspired kirigami crawlers with a fast-moving speed, agile maneuverability, and multimodal movements for wide environmental adaptability, and (2) the development of a new untethered soft robot-sensor platform for minimally invasive biomedical sensing.

4. MATERIALS AND METHODS

4.1. Fabrication of the Soft Kirigami Robot. PDMS (Sylgard 184, Dow Corning) with a base-to-curing agent ratio of 10:1 (by weight) and NdFeB microparticles (MQFP 15−7, Neo Magnequench) were mixed by a planetary mixer (AR-100, Thinky) at a weight ratio of 1:2. The mixture was spin-coated onto a substrate to obtain a thin film followed by curing the thin film at 60 °C for 12 h. The cured film was cut into designed kirigami patterns by using a laser cutter. A lab-made tensile strain stage was used to pre-stretch the patterned kirigami film. Then, the pre-stretched kirigami film was magnetized by a Halbach array with a central magnetic flux density of

https://doi.org/10.1021/acsami.3c13425
ACS Appl. Mater. Interfaces 2023, 15, 58839−58849

1.2 T for 30 min. After magnetization, the kirigami film was removed from the strain stage, and the tensile strain was released.

4.2. Fabrication of the Sensor Tag and Integrated Robot-Sensor Platform. The sensor tag consists of two parts: A screen-printed IDE and an inductive coil. To fabricate the IDE, polyimide (PI) tape (thickness: 0.06 mm) and toner transfer paper (Pulsar Professional fx) were used as the shadow mask and substrate, respectively. The PI tape was first laminated onto the toner transfer paper and then cut into a desired pattern using a mechanical plotter (CAMEO 4, Silhouette). The PI tape can be cut into the desired pattern without damaging the substrate (i.e., toner transfer paper). Conductive silver ink (Creative Materials Inc.) was screen-printed onto the toner transfer paper. After curing the silver ink at 60 °C for 2 h, the mask (PI tape) was removed. A mixture of PDMS (with the based to the curing agent ratio of 10:1 by weight) and $BaTiO_3$ (Nanostructured & Amorphous Materials, average particle size: 100−200 nm) at a weight ratio of 1:1 was spin-coated onto a substrate and then cured at 60 °C for 12 h. Afterward, the screen-printed IDE was laminated on the PDMS/$BaTiO_3$ thin film with the silver ink side facing downward. The printed IDE was then transferred from the toner transfer paper to the PDMS/$BaTiO_3$ thin film by immersion in deionized (DI) water. Note that the top coating of the toner transfer paper is water-soluble and serves as a sacrificial layer for transfer. A 100 pF capacitor and a 20-turn hand-wound coil made from copper wires (36 AWG, Remington Industries) were connected in parallel with the IDE, respectively. Finally, PDMS (base-to-curing agent ratio of 10:1 by weight) was spin-coated over the sensor tag to encapsulate the sensor. To integrate the soft kirigami robot and the IDE sensor, both components were placed within a mold, where a 1 mm gap was maintained between the robot's tail and the sensor's head. A small amount of PDMS precursor with a base-to-curing agent weight ratio of 10:1 was dispensed into the gap. Following this, the assembly underwent a curing process at 60 °C for 12 h to bond the robot and the wireless sensor together. Due to the good elasticity of PDMS and strong bonding of PDMS to the robot and sensor, the bonded connection between the robot and the sensor is sufficiently strong, ensuring the successful execution of monitoring tasks.

4.3. Friction Measurement of the Soft Kirigami Robot. The experimental setup for characterizing the COF of the kirigami robot in forward and backward directions is shown in Figure S11. The soft kirigami robot was fixed on a shelf to remain stretched. A materials testing system (858 Mini Bionix II, MTS mechanical tester) was connected to the soft kirigami robot via a thread through a pulley. During the testing process, the thread dragged the kirigami robot to move horizontally. The tensional force of the thread, which equals the friction exerted on the kirigami robot by the substrate, was recorded. Finally, the COF was calculated according to the recorded tensional force.

4.4. Magnetic Actuation Method. We employed a hand-held cylindrical magnet (DEX2, K&J Magnetics) to control the movements of the soft kirigami robot in various environments (Figure 6). For tasks requiring gap crossing, vertical crawling, inverted crawling, and subaquatic locomotion (Figure 6A−E), the magnet was positioned at a distance of 5 mm directly beneath the soft kirigami robot. The longitudinal axis of the magnet was aligned with the soft kirigami robot's length, and its south pole was oriented in the direction of the desired locomotion. A reciprocating actuation mode, as delineated in Figure 3E, was employed to facilitate the locomotion of the soft kirigami robot. To achieve directional control and steering of the soft kirigami robot, we placed the magnet 10 mm beneath the robot. The magnet's axis remained parallel to the length of the soft kirigami robot. The desired rotation of the soft kirigami robot was induced by rotating the magnet horizontally, prompting it to reorient itself toward the south pole of the magnet, as depicted in Figures 6F and S12A. Additionally, for the flipping motion of the soft kirigami robot, the magnet was again positioned 10 mm beneath the robot with its axis maintaining alignment with the robot's length. The flipping action was achieved by rotating the magnet in plane, as shown in Figures 6G and S12B.

4.5. Demonstrations with Ex Vivo Experiments. For the evaluation of the integrated robot-sensor platform, an ex vivo experiment was conducted using a pig esophagus procured from Nebraska Scientific. To provide the requisite magnetic flux density (170 mT) for the deployment and actuation of the robot-sensor platform, as well as to maintain a distance of 30 mm between the platform and the magnet, a hand-held magnet (BX8 × 8X8-N52, K&J Magnetics) was employed throughout the ex vivo testing procedure. During the ex vivo test, the pig esophagus was thoroughly immersed in water with a depth of 30 mm. Subsequently, the robot-sensor platform was actuated by the magnet, following the methodology outlined in Section 4.4, in order to execute a series of predetermined tasks. Following the successful actuation of the platform, the IDE sensor was immobilized in place and an additional segment of pig esophagus was interposed between the IDE sensor and the reader before performing the gastroesophageal reflux test. To assess the wireless sensor for impedance monitoring, an impedance analyzer (E4990A, Keysight) was connected to the reader. Diverse liquid mediums, encompassing water, milk, tea, and pH buffer solutions, were poured onto the IDE sensor to simulate conditions akin to gastroesophageal reflux. Subsequently, the resulting alterations in resistance were meticulously recorded by the impedance analyzer.

■ ASSOCIATED CONTENT

Supporting Information

The Supporting Information is available free of charge at https://pubs.acs.org/doi/10.1021/acsami.3c13425.

Analysis of magnetic torque and force; analysis of anisotropic frictional forces; size of the kirigami pattern; characterization of the IDE sensor and the coupling of the sensor and tag; anchor point locations for on−off actuation mode; comparison of two actuation modes; free body diagrams of the kirigami robot; experimental results for wireless impedance sensing when the distance between the IDE sensor and the reader is 40 mm; experimental results of the retention test; experimental results of the stability test; experimental results of the impact of magnetic shield layers on magnetic flux density; experimental setup for measuring the coefficient of friction; schematics of the actuation methods for steering and flipping; and table of comparison of magnetic soft robots (PDF)

Locomotion of the soft kirigami robot in different environments (Movie S1) (MOV)

Integrated soft robot-sensor platform for GERD monitoring (Movie S2) (MOV)

■ AUTHOR INFORMATION

Corresponding Author

Shanshan Yao − *Department of Mechanical Engineering, Stony Brook University, Stony Brook, New York 11794, United States;* orcid.org/0000-0002-2076-162X; Email: shanshan.yao@stonybrook.edu

Authors

Yizong Li − *Department of Mechanical Engineering, Stony Brook University, Stony Brook, New York 11794, United States;* orcid.org/0000-0002-8124-7624

Amro Halwah − *Department of Mechanical Engineering, Stony Brook University, Stony Brook, New York 11794, United States*

Shah R. A. Bhuiyan − *Department of Mechanical Engineering, Stony Brook University, Stony Brook, New York 11794, United States*

Complete contact information is available at:
https://pubs.acs.org/10.1021/acsami.3c13425

Author Contributions

Conceptualization: Y.L., S.Y. Methodology: Y.L., S.Y. Validation: Y.L., S.Y., A.H., S.R.A.B. Formal analysis: Y.L., S.Y. Supervision: S.Y. Writing—original draft: Y.L., S.Y., A.H. Writing—review and editing: Y.L., S.Y., A.H.

Funding

National Science Foundation (NSF) through Award 2238363 (S.Y.). Start-up fund at Stony Brook University (S.Y.).

Notes

The authors declare no competing financial interest.

■ ACKNOWLEDGMENTS

The authors gratefully acknowledge Professor Anurag Purwar at Stony Brook University for his help with laser patterning. The authors gratefully acknowledge Jian Zhuang, Jie Zhang, Aifen Tian, and Wei Ren at Xi'an Jiaotong University for their help during the project.

■ REFERENCES

(1) Yao, S.; Zhu, Y. Nanomaterial-Enabled Stretchable Conductors: Strategies, Materials and Devices. *Adv. Mater.* **2015**, *27*, 1480−1511.
(2) Li, C.; Cai, Y.; Hu, J.; Liu, J.; Dai, H.; Xu, Q.; Zhang, C.; Zhang, X.; Liu, K.; Kosinova, M. L.; et al. Sic/Graphene Film by Laser CVD as an Implantable Sensor Material for Dopamine Detection. *ACS Appl. Mater. Interfaces* **2023**, *15*, 27399−27410.
(3) Sun, J.; Wu, X.; Xiao, J.; Zhang, Y.; Ding, J.; Jiang, J.; Chen, Z.; Liu, X.; Wei, D.; Zhou, L.; Fan, H. Hydrogel-Integrated Multimodal Response as a Wearable and Implantable Bidirectional Interface for Biosensor and Therapeutic Electrostimulation. *ACS Appl. Mater. Interfaces* **2023**, *15*, 5897−5909.
(4) Mermel, L. A.; Allon, M.; Bouza, E.; Craven, D. E.; Flynn, P.; O'Grady, N. P.; Raad, I. I.; Rijnders, B. J.; Sherertz, R. J.; Warren, D. K. Clinical Practice Guidelines for the Diagnosis and Management of Intravascular Catheter-Related Infection: 2009 Update by the Infectious Diseases Society of America. *Clin. Infect. Dis.* **2009**, *49*, 1−45.
(5) Blot, F.; Brun-Buisson, C. Current Approaches to the Diagnosis and Prevention of Catheter-Related Infections. *Curr. Opin. Crit. Care* **1999**, *5*, 341−349.
(6) Gonzalez-Guillaumin, J. L.; Sadowski, D. C.; Kaler, K. V.; Mintchev, M. P. Ingestible Capsule for Impedance and Ph Monitoring in the Esophagus. *IEEE Trans. Biomed. Eng.* **2007**, *54*, 2231−2236.
(7) Mapara, S. S.; Patravale, V. B. Medical Capsule Robots: A Renaissance for Diagnostics, Drug Delivery and Surgical Treatment. *J. Controlled Release* **2017**, *261*, 337−351.
(8) Yim, S.; Sitti, M. Design and Rolling Locomotion of a Magnetically Actuated Soft Capsule Endoscope. *IEEE Trans. Rob.* **2012**, *28*, 183−194.
(9) Dong, P.; Song, Y.; Yu, S.; Zhang, Z.; Mallipattu, S. K.; Djurić, P. M.; Yao, S. Electromyogram-Based Lip-Reading Via Unobtrusive Dry Electrodes and Machine Learning Methods. *Small* **2023**, *19*, No. 2205058.
(10) Li, Y.; Liu, Y.; Bhuiyan, S. R. A.; Zhu, Y.; Yao, S. Printed Strain Sensors for on-Skin Electronics. *Small Struct.* **2022**, *3*, No. 2100131.
(11) Ceylan, H.; Giltinan, J.; Kozielski, K.; Sitti, M. Mobile Microrobots for Bioengineering Applications. *Lab Chip* **2017**, *17*, 1705−1724.
(12) Li, J.; de Ávila, B. E.-F.; Gao, W.; Zhang, L.; Wang, J. Micro/Nanorobots for Biomedicine: Delivery, Surgery, Sensing, and Detoxification. *Sci. Rob.* **2017**, *2*, No. eaam6431.
(13) Pozhitkova, A. V.; Kladko, D. V.; Vinnik, D. A.; Taskaev, S. V.; Vinogradov, V. V. Reprogrammable Soft Swimmers for Minimally Invasive Thrombus Extraction. *ACS Appl. Mater. Interfaces* **2022**, *14*, 23896−23908.
(14) Ze, Q.; Wu, S.; Nishikawa, J.; Dai, J.; Sun, Y.; Leanza, S.; Zemelka, C.; Novelino, L. S.; Paulino, G. H.; Zhao, R. R. Soft Robotic Origami Crawler. *Sci. Adv.* **2022**, *8*, No. eabm7834.
(15) Dong, Y.; Wang, L.; Xia, N.; Yang, Z.; Zhang, C.; Pan, C.; Jin, D.; Zhang, J.; Majidi, C.; Zhang, L. Untethered Small-Scale Magnetic Soft Robot with Programmable Magnetization and Integrated Multifunctional Modules. *Sci. Adv.* **2022**, *8*, No. eabn8932.
(16) Tian, J.; Li, M.; Han, Z.; Chen, Y.; Gu, X. D.; Ge, Q.; Chen, S. Conformal Topology Optimization of Multi-Material Ferromagnetic Soft Active Structures Using an Extended Level Set Method. *Comput. Methods Appl. Mech. Eng.* **2022**, *389*, No. 114394.
(17) Babaee, S.; Shi, Y.; Abbasalizadeh, S.; Tamang, S.; Hess, K.; Collins, J. E.; Ishida, K.; Lopes, A.; Williams, M.; Albaghdadi, M.; Hayward, A. M.; Traverso, G. Kirigami-Inspired Stents for Sustained Local Delivery of Therapeutics. *Nat. Mater.* **2021**, *20*, 1085−1092.
(18) Kim, Y.; Zhao, X. Magnetic Soft Materials and Robots. *Chem. Rev.* **2022**, *122*, 5317−5364.
(19) Pancaldi, L.; Noseda, L.; Dolev, A.; Fanelli, A.; Ghezzi, D.; Petruska, A. J.; Sakar, M. S. Locomotion of Sensor-Integrated Soft Robotic Devices inside Sub-Millimeter Arteries with Impaired Flow Conditions. *Adv. Intell. Syst.* **2022**, *4*, No. 2100247.
(20) Hu, W.; Lum, G. Z.; Mastrangeli, M.; Sitti, M. Small-Scale Soft-Bodied Robot with Multimodal Locomotion. *Nature* **2018**, *554*, 81−85.
(21) Ren, Z.; Zhang, R.; Soon, R. H.; Liu, Z.; Hu, W.; Onck, P. R.; Sitti, M. Soft-Bodied Adaptive Multimodal Locomotion Strategies in Fluid-Filled Confined Spaces. *Sci. Adv.* **2021**, *7*, No. eabh2022.
(22) Chen, S.; Chen, Y.; Yang, J.; Han, T.; Yao, S. Skin-Integrated Stretchable Actuators toward Skin-Compatible Haptic Feedback and Closed-Loop Human-Machine Interactions. *npj Flexible Electron.* **2023**, *7*, No. 1.
(23) Tian, J.; Zhao, X.; Gu, X. D.; Chen, S. In *Designing Conformal Ferromagnetic Soft Actuators Using Extended Level Set Methods (X-Lsm)*, ASME 2020 International Design Engineering Technical Conferences and Computers and Information in Engineering Conference; ASME, 2020.
(24) Tian, J.; Zhao, X.; Gu, X. D.; Chen, S. In *Designing Ferromagnetic Soft Robots (FerroSoRo) with Level-Set-Based Multi-physics Topology Optimization*, IEEE International Conference on Robotics and Automation (ICRA); IEEE: New York, 2020.
(25) Li, X.; Shang, Z.; Wang, Y.; Liu, J.; Xie, Y.; Li, J.; Liu, Y.; Gan, W. Programmable, Changeable, Origami Cellulose Films for Magnetically Controllable Soft Robots. *ACS Appl. Mater. Interfaces* **2023**, *15*, 28442−28452.
(26) Ma, C.; Chang, Y.; Wu, S.; Zhao, R. R. Deep Learning-Accelerated Designs of Tunable Magneto-Mechanical Metamaterials. *ACS Appl. Mater. Interfaces* **2022**, *14*, 33892−33902.
(27) Lu, H.; Zhang, M.; Yang, Y.; Huang, Q.; Fukuda, T.; Wang, Z.; Shen, Y. A Bioinspired Multilegged Soft Millirobot That Functions in Both Dry and Wet Conditions. *Nat. Commun.* **2018**, *9*, No. 3944.
(28) Lu, H.; Hong, Y.; Yang, Y.; Yang, Z.; Shen, Y. Battery-Less Soft Millirobot That Can Move, Sense, and Communicate Remotely by Coupling the Magnetic and Piezoelectric Effects. *Adv. Sci.* **2020**, *7*, No. 2000069.
(29) Wu, Y.; Dong, X.; Kim, J.-k.; Wang, C.; Sitti, M. Wireless Soft Millirobots for Climbing Three-Dimensional Surfaces in Confined Spaces. *Sci. Adv.* **2022**, *8*, No. eabn3431.
(30) Sun, J.; Bauman, L.; Yu, L.; Zhao, B. Gecko-and-Inchworm-Inspired Untethered Soft Robot for Climbing on Walls and Ceilings. *Cell Rep. Phys. Sci.* **2023**, *4*, No. 101241.
(31) Manafa, P. O.; Njoku, G. J.; Onyenekwe, C.; Ekuma-Okereke, O.; Nnadi, E.; Ebugosi, R.; Chukwuma, G.; Onah, E.; Chukwuanukwu, R.; Nwene, K.; et al. Assessment of Inflammatory and Cardiac Status of Echis Ocellatus Snake-Bite Victims in Jos Metropolis, Plateau State, Nigeria. *J. Adv. Med. Pharm. Sci.* **2020**, *22*, 20−30.

(32) Savidge, J. A. Extinction of an Island Forest Avifauna by an Introduced Snake. *Ecology* **1987**, *68*, 660−668.
(33) Dmi'el, R.; Borut, A. Thermal Behavior, Heat Exchange, and Metabolism in the Desert Snake Spalerosophis Cliffordi. *Physiol. Zool.* **1972**, *45*, 78−94.
(34) Hood, R. W.; Hood, J. Salvation on Sand Mountain: Snake Handling and Redemption in Southern Appalachia. *Appalachian Heritage* **1995**, *23*, 54−56.
(35) Kapp, K. J.; Yeatman, E. Microplastic Hotspots in the Snake and Lower Columbia Rivers: A Journey from the Greater Yellowstone Ecosystem to the Pacific Ocean. *Environ. Pollut.* **2018**, *241*, 1082−1090.
(36) Branyan, C.; Hatton, R. L.; Menguc, Y. Snake-Inspired Kirigami Skin for Lateral Undulation of a Soft Snake Robot. *IEEE Rob. Autom. Lett.* **2020**, *5*, 1728−1733.
(37) Rafsanjani, A.; Zhang, Y.; Liu, B.; Rubinstein, S. M.; Bertoldi, K. Kirigami Skins Make a Simple Soft Actuator Crawl. *Sci. Rob.* **2018**, *3*, No. eaar7555.
(38) Rus, D.; Tolley, M. T. Design, Fabrication and Control of Soft Robots. *Nature* **2015**, *521*, 467−475.
(39) Polygerinos, P.; Correll, N.; Morin, S. A.; Mosadegh, B.; Onal, C. D.; Petersen, K.; Cianchetti, M.; Tolley, M. T.; Shepherd, R. F. Soft Robotics: Review of Fluid-Driven Intrinsically Soft Devices; Manufacturing, Sensing, Control, and Applications in Human-Robot Interaction. *Adv. Eng. Mater.* **2017**, *19*, No. 1700016.
(40) Jayne, B. C. What Defines Different Modes of Snake Locomotion? *Integr. Comp. Biol.* **2020**, *60*, 156−170.
(41) Jayne, B. C. Kinematics of Terrestrial Snake Locomotion. *Copeia* **1986**, *1986*, 915−927.
(42) Jayne, B. C. Muscular Mechanisms of Snake Locomotion: An Electromyographic Study of the Sidewinding and Concertina Modes of Crotalus Cerastes, Nerodia Fasciata and Elaphe Obsoleta. *J. Exp. Biol.* **1988**, *140*, 1−33.
(43) Rieser, J. M.; Li, T.-D.; Tingle, J. L.; Goldman, D. I.; Mendelson, J. R., III Functional Consequences of Convergently Evolved Microscopic Skin Features on Snake Locomotion. *Proc. Natl. Acad. Sci. U.S.A.* **2021**, *118*, No. e2018264118.
(44) Baum, M. J.; Kovalev, A. E.; Michels, J.; Gorb, S. N. Anisotropic Friction of the Ventral Scales in the Snake Lampropeltis Getula Californiae. *Tribol. Lett.* **2014**, *54*, 139−150.
(45) Lim, A. W.; Talley, N. J.; Walker, M. M.; Storm, G.; Hua, S. Current Status and Advances in Esophageal Drug Delivery Technology: Influence of Physiological, Pathophysiological and Pharmaceutical Factors. *Drug Delivery* **2023**, *30*, No. 2219423.
(46) Lee, C.; Kim, M.; Kim, Y. J.; Hong, N.; Ryu, S.; Kim, H. J.; Kim, S. Soft Robot Review. *Int. J. Control Autom. Syst.* **2017**, *15*, 3−15.
(47) Săraru, E.-R.; Enciu, V.; Peagu, R.; Fierbinţeanu-Braticevici, C. Advances in the Diagnosis of Gerd. *Rom. J. Intern. Med.* **2021**, *59*, 3−9.
(48) Chhabra, P.; Ingole, N. Gastroesophageal Reflux Disease (Gerd): Highlighting Diagnosis, Treatment, and Lifestyle Changes. *Cureus* **2022**, *14*, No. e28563.
(49) El-Serag, H. B.; Sweet, S.; Winchester, C. C.; Dent, J. Update on the Epidemiology of Gastro-Oesophageal Reflux Disease: A Systematic Review. *Gut* **2014**, *63*, 871−880.
(50) Tabrez, E. S.; Hussain, A.; Rao, S.; Jagadeesh, A.; Peela, J. R.; Tabrez, S. S. Gastroesophageal Reflux Disease: A Review of Symptomatic Management. *Crit. Rev. Eukaryotic Gene Expression* **2018**, *28*, 87−92.
(51) Ruan, C.; Ong, K. G.; Mungle, C.; Paulose, M.; Nickl, N. J.; Grimes, C. A. A Wireless Ph Sensor Based on the Use of Salt-Independent Micro-Scale Polymer Spheres. *Sens. Actuators, B* **2003**, *96*, 61−69.
(52) Ativanichayaphong, T.; Wang, J.; Rao, S.; Tibbals, H.; Tang, S.-j.; Spechler, S.; Stephanou, H.; Chiao, J.-c. In *Development of an Implanted RFID Impedance Sensor for Detecting Gastroesophageal Reflux*, IEEE International Conference on RFID; IEEE: New York, 2007.
(53) Ativanichayaphong, T.; Huang, W.-D.; Wang, J.; Rao, S. M.; Tibbals, H.; Tang, S.-J.; Spechler, S.; Stephanou, H.; Chiao, J.-C. In *A Wireless Sensor for Detecting Gastroesophageal Reflux*, Biomedical Applications of Micro- and Nanoengineering III; SPIE: WA, 2006.
(54) Cao, H.; Landge, V.; Tata, U.; Seo, Y.-S.; Rao, S.; Tang, S.-J.; Tibbals, H. F.; Spechler, S.; Chiao, J.-C. An Implantable, Batteryless, and Wireless Capsule with Integrated Impedance and Ph Sensors for Gastroesophageal Reflux Monitoring. *IEEE Trans. Biomed. Eng.* **2012**, *59*, 3131−3139.
(55) Azzam, R. S.; Azzam, G. B.; Nasi, A. Wireless Ph Monitoring and Conventional Esophageal Ph Monitoring: Comparative Study of Discomfort, Limitations in Daily Activities and Complications. *ABCD, Arq. Bras. Cir. Dig.* **2021**, *34*, No. e1566.
(56) Yang, X.-J.; Gan, T.; Wang, L.; Liao, Z.; Tao, X.-H.; Shen, W.; Zhao, X.-Y. Wireless Esophageal Ph Capsule for Patients with Gastroesophageal Reflux Disease: A Multicenter Clinical Study. *World J. Gastroenterol.* **2014**, *20*, 14865−14874.
(57) Iluyomade, A.; Olowoyeye, A.; Fadahunsi, O.; Thomas, L.; Libend, C.; Ragunathan, K.; Fenster, J.; Vignesh, S. Interference with Daily Activities and Major Adverse Events During Esophageal Ph Monitoring with Bravo Wireless Capsule Versus Conventional Intranasal Catheter: A Systematic Review of Randomized Controlled Trials. *Dis. Esophagus* **2017**, *30*, 1−9.
(58) Savarino, E.; Bredenoord, A. J.; Fox, M.; Pandolfino, J. E.; Roman, S.; Gyawali, C. P. Advances in the Physiological Assessment and Diagnosis of Gerd. *Nat. Rev. Gastroenterol. Hepatol.* **2017**, *14*, 665−676.
(59) Huang, X.; Liu, Y.; Cheng, H.; Shin, W. J.; Fan, J. A.; Liu, Z.; Lu, C. J.; Kong, G. W.; Chen, K.; Patnaik, D.; et al. Materials and Designs for Wireless Epidermal Sensors of Hydration and Strain. *Adv. Funct. Mater.* **2014**, *24*, 3846−3854.
(60) Nopper, R.; Niekrawietz, R.; Reindl, L. Wireless Readout of Passive Lc Sensors. *IEEE Trans. Instrum. Meas.* **2010**, *59*, 2450−2457.
(61) Huang, Q.-A.; Dong, L.; Wang, L.-F. Lc Passive Wireless Sensors toward a Wireless Sensing Platform: Status, Prospects, and Challenges. *J. Microelectromech. Syst.* **2016**, *25*, 822−841.
(62) Li, Y.; Qi, Z.; Yang, J.; Zhou, M.; Zhang, X.; Ling, W.; Zhang, Y.; Wu, Z.; Wang, H.; Ning, B.; et al. Origami Ndfeb Flexible Magnetic Membranes with Enhanced Magnetism and Programmable Sequences of Polarities. *Adv. Funct. Mater.* **2019**, *29*, No. 1904977.
(63) He, H.; Stylogiannis, A.; Afshari, P.; Wiedemann, T.; Steiger, K.; Buehler, A.; Zakian, C.; Ntziachristos, V. Capsule Optoacoustic Endoscopy for Esophageal Imaging. *J. Biophotonics* **2019**, *12*, No. e201800439.
(64) Nelson, B. J.; Kaliakatsos, I. K.; Abbott, J. J. Microrobots for Minimally Invasive Medicine. *Annu. Rev. Biomed. Eng.* **2010**, *12*, 55−85.

https://doi.org/10.1021/acsami.3c13425
ACS Appl. Mater. Interfaces 2023, 15, 58839−58849